Solid-State Electronics 197 (2022) 108452

Contents lists available at ScienceDirect

Solid State Electronics

journal homepage: www.elsevier.com/locate/sse

# Bulk photovoltaic effect in partial overlap $MoSe_2$-$WSe_2$ van der Waals heterostructures: An *ab initio* quantum transport study☆

Jiang Cao *, Sara Fiore, Cedric Klinkert, Mathieu Luisier

*Integrated Systems Laboratory, ETH Zürich, Gloriastrasse 35, Zürich, 8092, Switzerland*

ARTICLE INFO

*Keywords:*
Quantum transport
Van der Waals heterostructure
Density functional theory
Optoelectronic device
Photodetector
Bulk photovoltaic effect

ABSTRACT

Two-dimensional (2-D) materials, especially transition metal dichalcogenides (TMDCs), have attracted great attention due to their unique properties and the vast possibility they offer when combined into van der Waals heterostructures (vdWHs), for example in optoelectronic applications. Although various photodetectors based on TMDC vdWHs have been successfully synthesized, an *ab initio* simulation framework dedicated to such devices is still missing. In this work, we investigate two photodetector designs based on $MoSe_2$-$WSe_2$ vdWHs through a recently developed approach combining density functional theory and quantum transport calculations. Geometries with a partial and total TMDC overlap are considered, with a p-doped (n-doped) left (right) extension and an intrinsic region in the middle. We show that the partial overlap structure supports a non-zero photo-current, even without a p–n junction, and gives rise to the bulk photovoltaic effect (BPVE). The present results provide an easy-to-fabricate guideline for engineering the BPVE in the TMDC vdWHs.

## 1. Introduction

Strong light–matter interactions in van der Waals hetero-structures (vdWHs) made of two-dimensional (2-D) materials, especially transition metal dichalcogenides (TMDCs) [1], have brought new perspectives to the research on optoelectronic devices. Stacking different TMDC monolayers into vdWHs gives rise to type-II band alignments with (quasi-)direct-gap [2]. This facilitates the generation of interlayer excitons, where electrons and holes are located in different monolayers, thus leading to extremely long lifetimes [3]. Lower electric fields are needed to separate interlayer electron–hole (e–h) pairs as compared to intralayer ones due to the reduced Coulomb interaction [2]. These advantages open the door for photodetectors with high responsivities at lower bias. In this context, several vdWHs made of mono- or few-layer TMDCs have been experimentally demonstrated to exhibit photovoltaic properties [4,5].

Homogeneous illumination on noncentrosymmetric crystals, e.g. $BaTiO_3$ and $LiNbO_3$ [6–8], yield steady-state photovoltaic current although there is no macroscopic electric field present. This phenomenon is known as the bulk photovoltaic effect (BPVE). Recent advances demonstrate novel methods to manipulate the BPVE by stacking crystals with different rotational symmetry and thus reducing the interfacial symmetry in the $WSe_2$/black phosphorus interface [9].

In the present Letter, we calculate the photo-current and quantum efficiency of two photodetector designs based on $MoSe_2$-$WSe_2$ vdWHs through combined density functional theory (DFT) and quantum transport simulations. Using these results, we are able to demonstrate the presence of BPVE in the partial overlap structure. In contrast, the full overlap structure only exhibits traditional photovoltaic effect. The present results offer a new easy-to-fabricate method to create the BPVE in symmetry-forbidden vdWHs by engineering the interface.

This paper is organized as follows. In Section 2, the modeling framework and the device structures are presented. Section 3 is devoted to the simulation results and discussions. Finally, conclusions are drawn in Section 4.

## 2. Method

All DFT calculations were performed with VASP using GGA-PBE [10] and including the non-local van der Waals correction through Grimme's DFT-D3 method [11]. The plane-wave Hamiltonian from VASP was then transformed into a basis of maximally localized Wannier functions (MLWFs) employing the wannier90 tool [12]. The resulting MLWF Hamiltonian was upscaled to a larger orthorhombic cell and repeated to construct the simulation domains with partial and total overlap [13].

The state-of-the-art atomistic quantum transport solver the OMEN [14] was employed for the simulations of the photo-current flowing through the vdWH device. The periodic boundary conditions along the

☆ The review of this paper was arranged by Francisco Gamiz.

* Corresponding author.
*E-mail addresses:* jiang.cao@iis.ee.ethz.ch (J. Cao), mluisier@iis.ee.ethz.ch (M. Luisier).

https://doi.org/10.1016/j.sse.2022.108452

Available online 17 September 2022

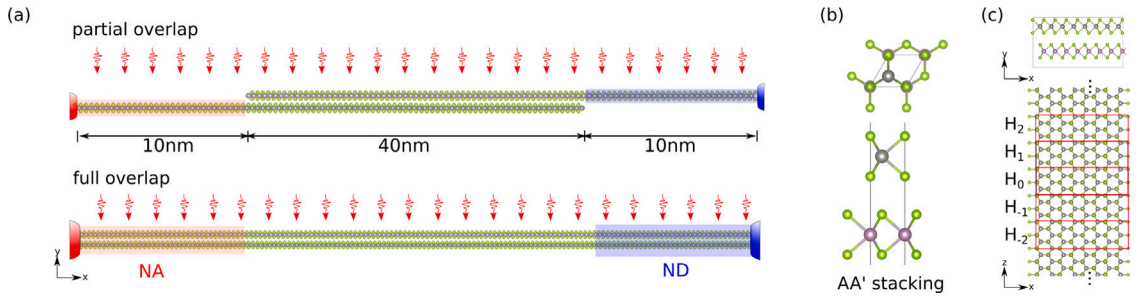


**Fig. 1.** (a) Photodiodes with partial (top) and full (bottom) monolayer overlap. The left (right) 10-nm region is doped with an acceptor (donor) density $N_A$ ($N_D$), respectively. (b) Unit cell of AA'-stacked $MoSe_2$-$WSe_2$ vdWH. (c) Orthorhombic unit cell used in the transport simulations.

$z$ direction were imposed to the Hamiltonian matrix by introducing a $k_z$-dependence according to

$$H(k_z) = \sum_{n\in\{-2,-1,0,1,2\}} H_{(n)} e^{ink_z\Delta_z}, \tag{1}$$

where $H_{(n)}$ describes the hoping Hamiltonian matrix connecting the central transport cell to its periodic replica situated at $z = z_0 + n\Delta_z$, with $\Delta_z$ being the width of the transport cell along $z$. Quantum transport based on the Non-equilibrium Green's Function (NEGF) formalism is at the core of our device simulations [15]

$$\begin{aligned} &\Big(E\cdot I - H(k_z) - \Sigma^R(E,k_z)\Big)\cdot G^R(E,k_z) = I, \\ &G^{\gtrless}(E,k_z) = G^R(E,k_z)\cdot\Sigma^{\gtrless}(E,k_z)\cdot G^A(E,k_z), \end{aligned} \tag{2}$$

where $I$ is the identity matrix, and $E$ the electron energy. The $G^R$, $G^A = (G^R)^\dagger$, $G^<$, and $G^>$ quantities are the retarded, advanced, lesser, and greater Green's functions, respectively. The $\Sigma^{R,\gtrless}$ are self-energy matrices that contain a boundary $\Sigma^{R,\gtrless B}$ and a scattering $\Sigma^{R,\gtrless S}$ term. The boundary self-energy is calculated numerically assuming periodic repetition of the boundary slab.

To take into account the light–matter interactions, a dedicated scattering self-energy and simulation framework has been implemented in our recent work [16]. The electron–photon (e–phot) coupling matrix elements is obtained from the momentum operator [12]

$$\vec{p}_{nm}(\vec{R}) = \frac{im_0}{\hbar}\left\langle \vec{R}, n\right| [H,\vec{r}] \left|\vec{0}, m\right\rangle, \tag{3}$$

where $\vec{R}$ is a lattice vector connecting the unit cell located at the origin $\vec{0}$ to its periodic replica at $\vec{R}$, $i$ is the imaginary unit, whereas the indices $n$ and $m$ run over the MLWFs. The e–phot coupling matrix elements are then defined as $M^{\lambda}_{n,m}(k_z) = c_0\vec{e}_{\vec{q}\lambda}\cdot\vec{p}_{nm}(k_z)$, where $c_0$ denotes the speed of light, $\vec{e}_{\vec{q}\lambda}$ the polarization unit vector of the photon mode $\lambda$ with wavevector $\vec{q}$, and $\vec{p}_{nm}(\vec{k}) = \sum_{\vec{R}} e^{-i\vec{k}\cdot\vec{R}}\vec{p}_{nm}(\vec{R})$. In our calculations, we consider a monochromatic light beam that enters the 2-D vdWHs orthogonal to the surface with a power density $J$ and a photon energy $E_{ph}$. The e–phot scattering self-energy is given by [16]

$$\begin{aligned} \Sigma^{\gtrless,S}_{n,m}(E,k_z) = \frac{e^2\hbar^2}{2\epsilon_0 m_0^2 c_0^3}\sum_{\lambda,l_1,l_2}\frac{J}{E_{ph}^2} M^{\lambda}_{n,l_1}(k_z)M^{\lambda}_{l_1,m}(k_z)\times \\ \left[G^{\gtrless}_{l_1,l_2}(E\mp E_{ph},k_z) + G^{\gtrless}_{l_1,l_2}(E\pm E_{ph},k_z)\right], \end{aligned} \tag{4}$$

where $e$ is the elementary charge, $\epsilon_0$ the vacuum permittivity, $m_0$ the rest mass of electron, and $\hbar$ the reduced Planck constant. After solving the NEGF equations, the photo-excited current $I$ flowing through the vdWH device can be computed from the $G^{\gtrless}$ with an atomistic resolution. Furthermore, these results can be used to evaluate the optical absorption coefficient $\alpha$ under the random phase approximation, as

$$\alpha(E_{ph}) = \sum_{k_z}\mathrm{Re}\left\{\frac{i}{2}[\Pi^>(E_{ph},k_z) - \Pi^<(E_{ph},k_z)]\right\}, \tag{5}$$

where $\Pi^{\gtrless}$ denotes the polarizability [17]

$$\begin{aligned} \Pi^{\gtrless}(E_{ph},k_z) = \sum_{n,m,l_1,l_2}\int\frac{dE}{2\pi}\Big[M^{\lambda}_{n,m}G^{\gtrless}_{m,l_1}(E,k_z)\times \\ M^{\lambda}_{l_1,l_2}G^{\gtrless}_{l_2,n}(E-E_{ph},k_z)\Big]. \end{aligned} \tag{6}$$

We study two typical device structures shown in Fig. 1. Geometries with a partial and full TMDC overlap are considered, with a p-doped (n-doped) left (right) extension and an intrinsic region in the middle. The built-in potential drops between the left and right contacts is denoted by $V_{bi}$. For the partial overlap systems, only the $MoSe_2$ ($WSe_2$) monolayer is connected to the right (left) contact. This is done by removing the missing atoms in Fig. 1(a) from the structure, from the Hamiltonian matrix, and from the electron–photon coupling matrix. For the full overlap systems, both $MoSe_2$ and $WSe_2$ layers are connected to the left and right contacts.

A reference potential is obtained from a ballistic, self-consistent Schrödinger–Poisson equation without light illumination using reference doping concentrations of $N_D = N_A = 6\times10^{12}$ cm$^{-2}$. For the simulations of different $V_{bi}$, we scale the reference potential by a constant factor to obtain the desired potential drop between the left and right contacts. Next, we apply the potential in the simulation with the e–phot self-energy to compute the photo-current. Since the photo-generated charge density is low, we neglect its perturbation on the potential. Hence, there is no self-consistent solution of the Poisson equation at this stage.

## 3. Results

Fig. 2(a) shows the band structure of the $MoSe_2$-$WSe_2$ vdWH. At the K point, the (CBM+1) and the (VBM) wavefunctions are strongly localized inside the $WSe_2$ layer, while the CBM is localized inside the $MoSe_2$ layer. We find that the wavefunction corresponding to second highest valence band (VBM-1) is delocalized over both monolayer. Fig. 2(b) reports the absorption coefficient $\alpha$ as a function of the photon energy $E_{ph}$. It is given for the $MoSe_2$ monolayer, $WSe_2$ monolayer, and the vdWH. We notice that the onset of $\alpha$ for the vdWH is lower than for both monolayers, indicating the presence of interlayer absorption. By inspecting Eqs. (5) and (6), we see that non-zero contribution to $\alpha$ can stem from an interlayer coupling in either the Green's function $G^{\gtrless}_{n,m}$ and/or e–phot coupling $M_{n,m}$. In this case, by artificially setting the interlayer elements to zero, we observe that the non-zero contribution mostly comes from the interlayer coupling in the Hamiltonian and therefore in $G^{\gtrless}_{n,m}$ rather than directly from the e–phot coupling.

Fig. 3 presents the quantum efficiency (QE) of the different photodetector designs as a function of the photon energy $E_{ph}$ and the built-in potential $V_{bi}$. The QE is defined as the number of e–h pairs contributing to the photo-current $I$ divided by the number of incident photons: *i.e.*, QE= $\frac{I/e}{LJ/E_{ph}}$, with $L = 60$ nm the total illuminated length. For the full overlap structure, the highest QE happens at $E_{ph} = 1.9$ eV and no photo-current is generated with $V_{bi} = 0$. This zero current occurs because

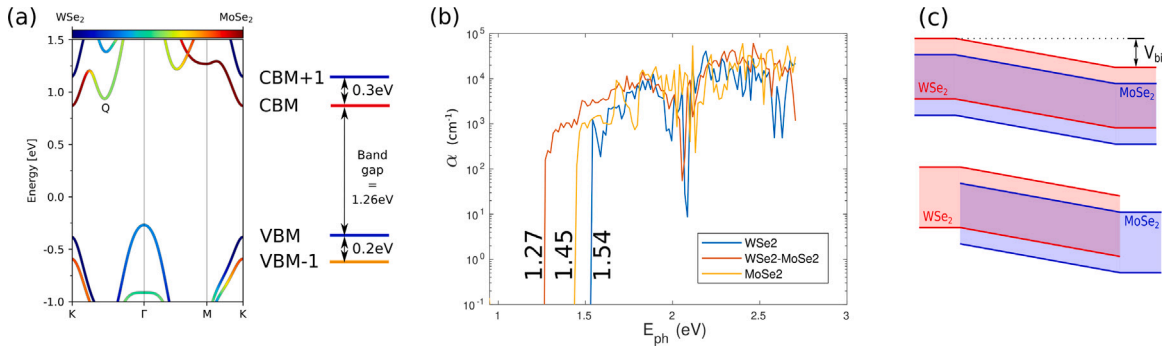


**Fig. 2.** (a) Partial bandstructure of an AA'-stacked $MoSe_2$-$WSe_2$ vdWH projected onto the orbitals of $MoSe_2$ (red) and $WSe_2$ (blue). (b) Calculated absorption spectra of the $MoSe_2$-$WSe_2$ vdWH and of its constituent monolayers. (c) Sketch of band diagram along axis connecting the n- and p-side of the photodiode. $V_{bi}$ denotes the built-in potential. (For interpretation of the references to color in this figure legend, the reader is referred to the web version of this article.)

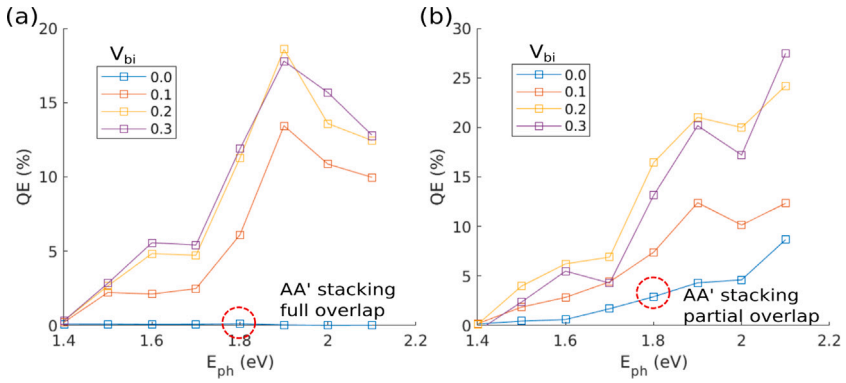


**Fig. 3.** (a) Quantum efficiency (QE) of the $MoSe_2$-$WSe_2$ vdWH photodiode with a full overlap structure for photon energies $E_{ph}$=1.4–2.2 eV and built-in potentials $V_{bi}$=0–0.3 V. The doping concentrations corresponding to the $V_{bi}$ are $N_A = N_D = 0, 4, 7, 9 \times 10^{10}$ cm$^{-2}$. (b) Same as (a), but for the partial overlap structure.

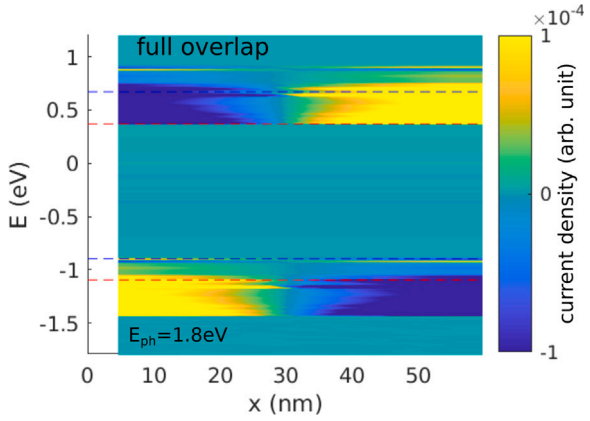


**Fig. 4.** Energy-resolved photo-current density in the full overlap device structure at $V_{bi}$=0, and $E_{ph}$=1.8 eV. The dashed lines represent CBM+1, CBM, VBM, and VBM-1.

the full overlap structure is symmetric under flat band condition: the current flows along the right and left directions cancel each other, as shown by the electron-energy-resolved current density in Fig. 4.

For the partial overlap structure, a non-zero QE with $V_{bi} = 0$ arises because the two monolayers are no longer symmetrically connected to the p- and n-type contacts. To shed light on the origin of this net current, we decomposed the photo-current flowing along the device into 4 intra- and inter-layer components shown in Fig. 5(a). The weak interlayer currents prove that the photo-excited charges mostly stay inside the layer where they are created. For the left and right non-overlapping regions, the interlayer currents are exactly zero, as expected. The current inside each layer gradually increases towards the contact to which the layer is connected. By selecting the energy range of the photo-current, we can proper separate its electron and hole contributions, which are plotted in Figs. 5 (b) and (c). We notice that the electron current is mostly located inside the $MoSe_2$ layer, while the hole current is more equally distributed. The electrons inside the $WSe_2$ layer generate a negative current towards the left because they can only be absorbed by the p-type contact to which this layer is connected. However, the electrons inside the $MoSe_2$ layer give rise to a positive current because they are absorbed by the n-type contact. Similarly, the holes inside the $MoSe_2$ layer generate negative current that increases towards the n-type contact on the right, while the holes in the $WSe_2$ layer produce a positive current. Since the charges mostly remain in the layer where they are created, the difference between the electron and hole currents in each layer originates from the photo-excited interlayer e–h pairs. Fig. 6 presents the energy-resolved photocurrent density along the device illustrating the e–h pair generation inside the different regions of the device with partial overlap.

## 4. Conclusion

In this work, we employed a recently developed electron–photon scattering model within the framework of NEGF to study different photodetector designs based on 2-D TMDC vdWHs. We demonstrated that a structure with partial overlap exhibits the BPVE thus generating high photo-responsivity at zero built-in potential and voltage bias. The non-zero photo-current was explained by a generation of interlayer electron–hole pairs and the symmetry breaking structure. We observed photo-responsivity in the full overlap structure only when non-zero built-in potential is applied, thus showing the traditional photovoltaic effect. The present results offer design guideline for engineering easy-to-fabricate photodetectors based on 2-D TMDC vdWHs that cooperatively exploit the BPVE and traditional photovoltaic effect.

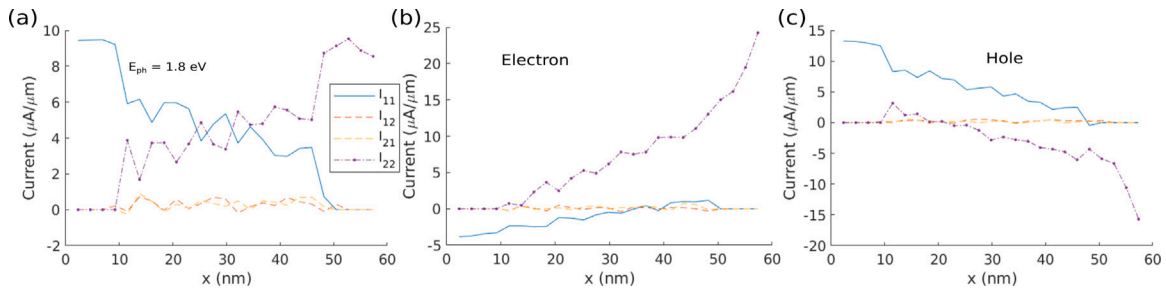


**Fig. 5.** (a) Photo-currents flowing through a $MoSe_2$-$WSe_2$ photodiode with partial overlap at $V_{bi} = 0$ and $E_{ph}$=1.8 eV. $I_{11}$ ($I_{22}$) is the current flowing between atoms in the $WSe_2$ ($MoSe_2$) layer, while $I_{12}$ ($I_{21}$) is the inter-layer current flowing from the $WSe_2$ ($MoSe_2$) to the $MoSe_2$ ($WSe_2$) monolayer. (b) Same as (a), but only for electrons. (c) Same as (a), but only for holes.

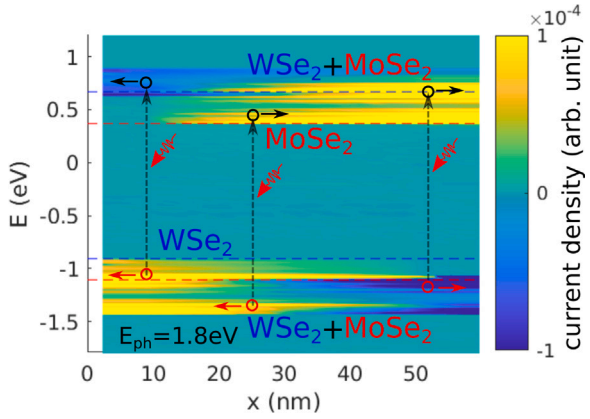


**Fig. 6.** Energy-resolved photo-current density in the partial overlap device structure at $V_{bi}$=0 and $E_{ph}$=1.8 eV. The dashed lines represent CBM+1, CBM, VBM, and VBM-1.

## Declaration of competing interest

The authors declare that they have no known competing financial interests or personal relationships that could have appeared to influence the work reported in this paper.

## Data availability

Data will be made available on request.

## Acknowledgments

This work was supported by the Marie Skłodowska-Curie, Switzerland Grant No. 885893, and by a grant from the Swiss National Supercomputing Centre (CSCS) under Project s1119.

## References

[1] Lee C-H, Lee G-H, van der Zande AM, Chen W, Li Y, Han M, et al. Atomically thin p–n junctions with van der Waals heterointerfaces. Nat Nanotechnol 2014;9(9):676–81.

[2] Lin K-Q. A roadmap for interlayer excitons. Light: Sci Appl 2021;10(1):99.

[3] Rivera P, Seyler KL, Yu H, Schaibley JR, Yan J, Mandrus DG, et al. Valley-polarized exciton dynamics in a 2D semiconductor heterostructure. Science 2016;351(6274):688–91. http://dx.doi.org/10.1126/science.aac7820.

[4] Flöry N, Jain A, Bharadwaj P, Parzefall M, Taniguchi T, Watanabe K, et al. A WSe2/MoSe2 heterostructure photovoltaic device. Appl Phys Lett 2015;107(12):123106. http://dx.doi.org/10.1063/1.4931621.

[5] Choi W, Akhtar I, Kang D, Lee Y-j, Jung J, Kim YH, et al. Optoelectronics of multijunction heterostructures of transition metal dichalcogenides. Nano Lett 2020;20(3):1934–43. http://dx.doi.org/10.1021/acs.nanolett.9b05212.

[6] Chynoweth AG. Surface space-charge layers in barium titanate. Phys Rev 1956;102:705–14. http://dx.doi.org/10.1103/PhysRev.102.705.

[7] Chen FS. Optically induced change of refractive indices in LiNbO3 and LiTaO3. J Appl Phys 1969;40(8):3389–96. http://dx.doi.org/10.1063/1.1658195.

[8] Glass AM, von der Linde D, Negran TJ. High-voltage bulk photovoltaic effect and the photorefractive process in LiNbO3. Appl Phys Lett 1974;25(4):233–5. http://dx.doi.org/10.1063/1.1655453.

[9] Akamatsu T, Ideue T, Zhou L, Dong Y, Kitamura S, Yoshii M, et al. A van der Waals interface that creates in-plane polarization and a spontaneous photovoltaic effect. Science 2021;372(6537):68–72. http://dx.doi.org/10.1126/science.aaz9146.

[10] Kresse G, Furthmüller J. Efficient iterative schemes for ab initio total-energy calculations using a plane-wave basis set. Phys Rev B 1996;54:11169–86. http://dx.doi.org/10.1103/PhysRevB.54.11169.

[11] Grimme S, Antony J, Ehrlich S, Krieg H. A consistent and accurate ab initio parametrization of density functional dispersion correction (DFT-D) for the 94 elements H-Pu. J Chem Phys 2010;132(15):154104. http://dx.doi.org/10.1063/1.3382344.

[12] Mostofi AA, Yates JR, Pizzi G, Lee Y-S, Souza I, Vanderbilt D, et al. An updated version of Wannier90: A tool for obtaining maximally-localised Wannier functions. Comput Phys Comm 2014;185(8):2309–10. http://dx.doi.org/10.1016/j.cpc.2014.05.003.

[13] Szabó Á, Rhyner R, Luisier M. Ab initio simulation of single- and few-layer $MoS_2$ transistors: Effect of electron-phonon scattering. Phys Rev B 2015;92:035435. http://dx.doi.org/10.1103/PhysRevB.92.035435.

[14] Luisier M, Schenk A, Fichtner W, Klimeck G. Atomistic simulation of nanowires in the $sp^3d^5s^*$ tight-binding formalism: From boundary conditions to strain calculations. Phys Rev B 2006;74:205323. http://dx.doi.org/10.1103/PhysRevB.74.205323.

[15] Luisier M, Klimeck G. Atomistic full-band simulations of silicon nanowire transistors: Effects of electron-phonon scattering. Phys Rev B 2009;80:155430. http://dx.doi.org/10.1103/PhysRevB.80.155430.

[16] Cao J, Fiore S, Klinkert C, Vetsch N, Luisier M. Light-matter interactions in van der waals photodiodes from first principles. Phys Rev B 2022;106:035306. http://dx.doi.org/10.1103/PhysRevB.106.035306.

[17] Aeberhard U. Photovoltaics at the mesoscale: Insights from quantum-kinetic simulation. J Phys D: Appl Phys 2018;51(32):323002. http://dx.doi.org/10.1088/1361-6463/aacf74.